electronics

IMPACT FACTOR 2.9

CITESCORE 7.0

Article

Computational Design and Analysis of a High-Isolation 5G MIMO Antenna Using a Binary GWO-Optimized Pixelated Metasurface

Mehmet Ülgü, Muharrem Karaaslan, Ahmet Atcı, Lulu Wang and Olcay Altıntaş

MDPI

https://doi.org/10.3390/electronics15081625 electronics

MDPI

Article

Computational Design and Analysis of a High-Isolation 5G MIMO Antenna Using a Binary GWO-Optimized Pixelated Metasurface

Mehmet Ülgü [1,2,*], Muharrem Karaaslan [2], Ahmet Atcı [2], Lulu Wang [3] and Olcay Altıntaş [4]

1 Department of Electrical and Energy, Vocational School of Tufanbeyli, Cukurova University, Adana 01250, Türkiye
2 Department of Electrical and Electronics Engineering, Faculty of Engineering and Natural Sciences, Iskenderun Technical University, Hatay 31200, Türkiye
3 Department of Engineering, Reykjavik University, 102 Reykjavik, Iceland
4 Department of Avionics, Faculty of Aeronautics and Astronautics, Iskenderun Technical University, Hatay 31200, Türkiye
* Correspondence: mulgu@cu.edu.tr

Abstract

Compact 5G millimeter-wave (mm-Wave) multiple-input multiple-output (MIMO) systems face a serious challenge as high isolation is required for high spectral efficiency. This paper presents a novel computational design framework for enhancing the isolation of a two-port ultra-wideband (UWB) MIMO antenna, specifically targeting the 5G n257 band (26.5–29.5 GHz). A pixelated metasurface is presented and optimized with the help of a binary-coded Grey Wolf Optimizer (B-GWO) algorithm through a MATLAB-Computer Simulation Technology (CST) co-simulation interface, which is used in contrast to some conventional decoupling structures. A Geometric Mirror Symmetry method is used to accelerate the optimization process, which halves the number of optimization variables and significantly reduces the computational load. Crucially, this symmetry is also a fundamental requirement to ensure that the reflection coefficients (S_{11}, S_{22}) of the antennas remain identical. The proposed design achieves isolation levels better than 20 dB across the entire target band, reaching a peak isolation of 32.58 dB at 28.67 GHz, while maintaining reflection coefficients (S_{11}, S_{22}) below -10 dB. The MIMO diversity performance is comprehensively validated with an Envelope Correlation Coefficient (ECC) < 0.005, a Diversity Gain (DG) of 9.99 dB, and a Total Active Reflection Coefficient (TARC) < -10 dB. Moreover, the suppression of surface waves enhances the realized gain to 4.51 dBi, providing a 0.57 dB improvement over the reference antenna. In addition, an equivalent passive RLC circuit model is constructed to observe the physical process of the pixelated surface, which shows the optimized structure as a band stop filter at the coupling frequency. The high correlation of the Equivalent Circuit Model and full-wave simulation outcomes confirms that the suggested design procedure is a strong verification alternative to physical fabrication.

Keywords: MIMO; pixelated metasurface; Binary Grey Wolf Optimizer; mutual coupling; millimeter-wave; 5G

Check for updates

Received: 9 February 2026
Revised: 15 March 2026
Accepted: 24 March 2026
Published: 14 April 2026

1. Introduction

The high dynamic development of fifth-generation (5G) wireless communication systems has led to the need for small and high-performance antenna designs that work in the mm-Wave spectrum. Achieving high data rates in the 28 GHz band requires MIMO technology [1]. However, diversity gain and system performance are seriously impaired because the elements of the antenna are closely spaced in compact devices, resulting in high mutual coupling. In parallel, broadband microstrip antenna designs operating at 28 GHz have been developed to address the specific bandwidth and high-speed demands of modern 5G systems [2]. Furthermore, electromagnetic bandgap (EBG) structures have been integrated into mm-Wave MIMO antennas for wearable applications to enhance isolation and minimize the specific absorption rate (SAR) at 28 GHz [3]. Nevertheless, systematic reviews indicate that with device miniaturization, the reduction in electromagnetic interference remains the main limiting factor in meeting theoretical throughput limits [4].

To overcome these challenges, early studies emphasized geometric manipulation and decoupling networks. Some researchers have successfully reduced mutual coupling significantly by incorporating defected ground planes (DGSs) into MIMO antenna designs. Elalaouy et al. achieved an isolation level below 27.9 dB in their two-port MIMO antenna study without using any decoupling elements [5]. Khalid et al., on the other hand, suppressed mutual coupling in four-port MIMO antenna designs by employing DGSs. In the antenna structure proposed for 5G applications, they achieved a peak gain of 8.3 dBi within the operating frequency band [6]. Bhattacharya et al. obtained inter-element isolation in UWB MIMO antenna designs by combining a DGS with a fractal-shaped geometry [7]. On the other hand, researchers have achieved coupling reduction by integrating decoupler structures into MIMO antenna systems for different scenarios. Rao et al. observed mutual coupling lower than -18.2 dB between Tx and Rx pairs by using an inverted mushroom structure for a full-duplex MIMO system [8]. Wu et al. proposed an array antenna decoupling surface architecture by utilizing small metallic patches to suppress unwanted coupling waves in large-scale array antenna systems [9]. Ahmed et al. reported an acceptable mutual coupling level of around 37 dB by employing metamaterial surface absorbers, even when the spacing in the antenna array structure was reduced [10]. Li et al. achieved both isolation and radiation pattern control by using a multiport optimization method combined with decoupling and pattern shaping design [11]. Similarly, Zhang et al. reduced mutual coupling, obtained a wider bandwidth, and preserved the radiation pattern through an integrated radiator and decoupler surface structure [12]. In addition to these studies, Rao et al. successfully controlled coupling using reconfigurable intelligent surface structures consisting of a 5×5 subelement structure, and achieved wide-angle passive beamforming [13].

In the field of antenna design, there has been a growing interest in optimization techniques based on computational intelligence. These nature-inspired methods, which are gradually replacing conventional optimization techniques, make it more feasible to approach optimal levels for multiple design variables simultaneously [14–18]. For example, Song et al. integrated a particle swarm optimization-based metasurface structure into an array antenna configuration for 5G applications and achieved a gain of 27 dB at 28 GHz [19]. On the other hand, Nath et al. successfully reduced the sidelobe level in thinned planar antenna array designs by employing the almost difference sets method [20]. Koveleva et al. designed and optimized pixelated metasurface structures using the cross-entropy method and achieved a transmission magnitude above 0.9 in the X band [21].

Broadband topological optimization studies of RF antennas on dielectric substrates have led to the popularization of pixelated architectures [22]. Through this innovative structural development, the placement of different pixel shapes within antenna structures has enabled the effective use of the Binary Particle Swarm Optimization (BPSO) method for IoT devices [23]. In addition, pixelated deflected ground structure studies have also benefited from this optimization method (BPSO) [24]. Moreover, BPSO is a method used for reducing mutual coupling between antennas by means of pixelated parasitic element designs [25]. Zhou et al., Zheng and Li, and Rodrigo et al. demonstrated that compact MIMO antenna designs using parasitic pixel layers can enable frequency, radiation pattern, and polarization reconfiguration [26–28]. Furthermore, Jiang et al. developed pixel antenna structures using an optimization approach based on the Perturbation Sensitivity Analysis method [29]. Song et al. optimized this pixel antenna structure concept using a genetic algorithm (GA) technique to reconfigure the operating frequency [30]. Qiao et al. designed pixel antenna structures by binarizing the pixels and employing the Method of Moving Asymptotes [31]. Moreover, multiport pixel antenna optimization using GA [32] and Characteristic Mode Analysis [33] has been proposed to identify optimal feed positions, thereby eliminating the need for complex decoupling networks. In addition to these studies, pixel-based designs have been integrated into fluid antenna systems adapted for smart city infrastructures to overcome switching latency limitations [34,35]. Beyond conventional optimization methods, The B-GWO method has also been employed by researchers to optimize complex pixel patterns and to achieve tunable ultra-wideband characteristics [36].

In this study, a computationally driven design approach is presented to enhance the isolation performance of a compact two-port UWB MIMO antenna operating in the 5G mm-Wave n257 band. A pixelated metasurface is placed between the antenna elements and optimized using a B-GWO algorithm through a MATLAB–CST co-simulation framework. To reduce the optimization complexity, a Geometric Mirror Symmetry strategy is adopted. It enables the number of optimization variables to be decreased while preserving identical input matching characteristics for both ports. The optimized pixelated surface effectively suppresses surface wave propagation and significantly reduces mutual coupling over the target frequency band. In addition to isolation enhancement, the proposed approach improves radiation performance without introducing additional insertion losses. The MIMO system's performance is further validated using standard metrics such as ECC and TARC, demonstrating the suitability of the proposed antenna system for compact and dense 5G mm-Wave applications.

2. Design Process

2.1. Antenna Design

The proposed MIMO antenna system consists of two planar rectangular monopole elements designed to operate in the 5G n257 frequency band. The antenna is constructed on a low-loss Rogers RT5880 substrate with a relative permittivity of $\varepsilon_r = 2.2$, a loss tangent of $\tan\delta = 0.0009$, and a substrate thickness of $h = 0.508$ mm. All conductive parts of the proposed design are implemented using copper with a thickness of $t = 0.035$ mm and a conductivity of $\sigma = 5.8 \times 10^7$ S/m. This substrate was selected to reduce dielectric losses, which is important to ensure high radiation efficiency at millimeter-wave frequencies. The radiating element is a simple rectangular patch fed by a 50 Ω microstrip line. A partial (truncated) ground plane is used on the bottom layer in order to improve the impedance bandwidth. The gap between the radiating element and the ground edge is also a matching mechanism where the capacitive coupling is optimized to ensure that the value of S_{11} is less than -10 dB across the required bandwidth. The two elements are separated by an edge-to-edge spacing (D) of 4 mm (0.37λ). To eliminate mutual coupling, a pixelated decoupling surface is incorporated in the inter-element region as illustrated in Figure 1.

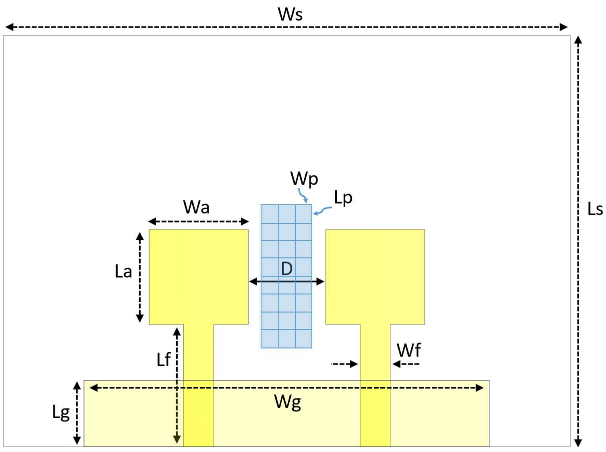

Figure 1. Geometry of the proposed 2-port UWB MIMO antenna with the optimized pixelated decoupling surface.

The decoupling structure is a 3×8 grid of rectangular pixels. The resulting optimized topology, achieved using the B-GWO algorithm, is implemented as an array of pixelated copper patches (parasitic elements) to control the near-field coupling currents. The dimensions of the optimized antenna system are shown in Table 1.

Table 1. The dimensions of the optimized antenna system (in mm).

Parameter	Dimension	Parameter	Dimension	Parameter	Dimension
W_s	29.2	W_a	5.1	W_g	19.3
L_s	21.2	L_a	4.9	L_g	6
h	0.508	W_f	1.55	W_p	0.7
t	0.035	L_f	6.3	L_p	1

2.2. Proposed Computational Design Framework

In this study, the isolation surface of the proposed MIMO antenna system was optimized without any manual intervention using a fully automated co-simulation interface established between MATLAB R2024b and CST Studio Suite 2021. The design process is managed by the B-GWO algorithm, a meta-heuristic method. The architecture and optimization strategies of the proposed framework are detailed below.

The optimization loop is implemented through a dynamic ActiveX (COM) connection between the main code executing in the MATLAB environment and the electromagnetic solver, CST. MATLAB acts as an optimization agent; at every step, it generates a new pixel topology (binary bit sequence). This topology is subsequently transferred to CST through Visual Basic for Applications (VBA) commands. On the CST side, the following operations are performed automatically in sequence:

- Updating the 3D model;
- Re-generating the mesh structure;
- Running a full-wave simulation using the Time Domain Solver.

Once the simulation is complete, the resulting S-parameters (S_{11}, S_{21}, S_{22}) are exported in ASCII format, read by MATLAB, and used in performance evaluation. This proposed flowchart is illustrated in Figure 2.

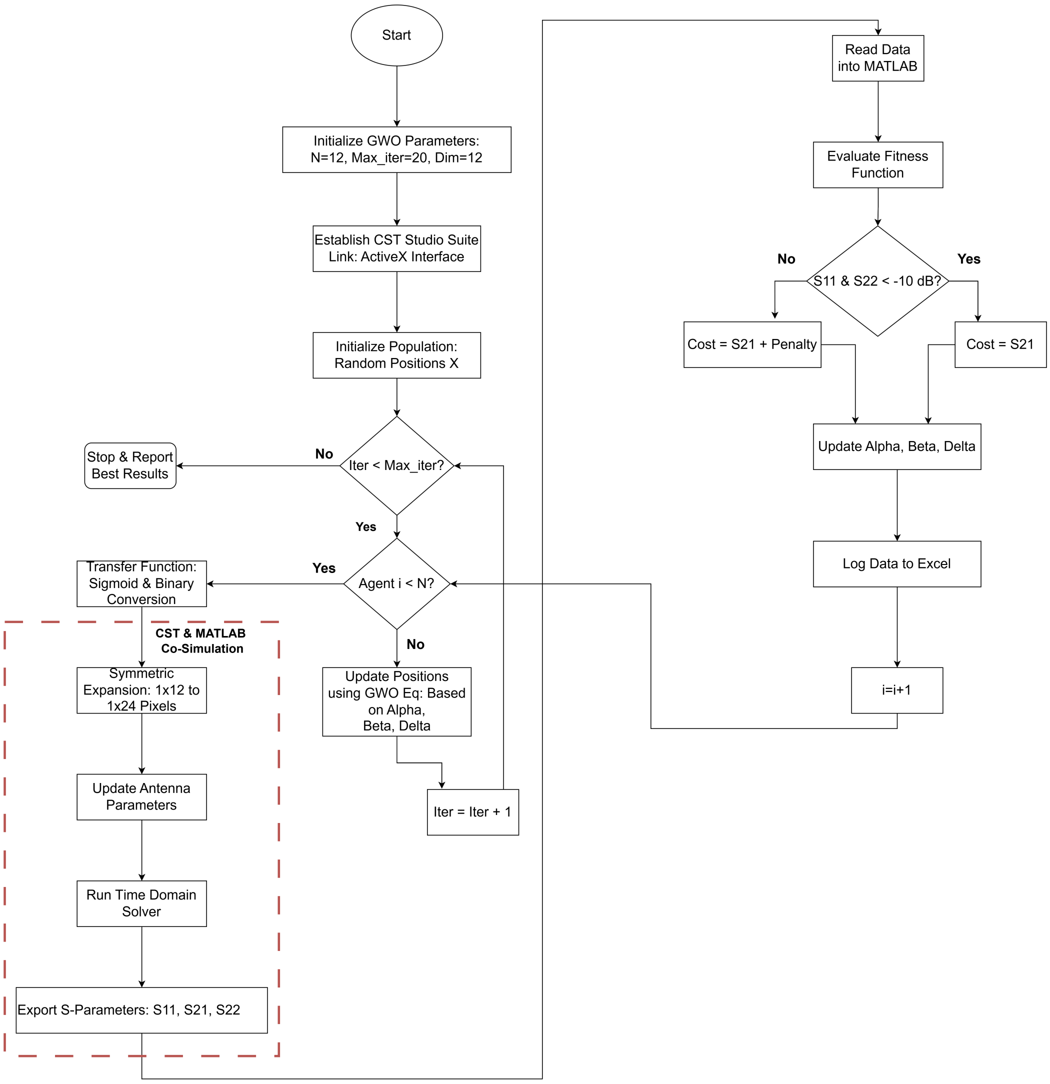

Figure 2. Flowchart of the proposed BGWO-CST co-simulation optimization process.

All computational processes and full-wave co-simulations were performed on a standard computing system equipped with an Intel Core i5-10400H CPU @ 2.50 GHz and 16 GB of RAM. Under these computing conditions, the B-GWO algorithm converged rapidly, and the entire optimization process for 20 iterations took approximately 16 h.

The core logical structure was independently designed and verified to ensure the integrity of the optimization process. Subsequently, the MATLAB scripts utilized for the B-GWO routine were refined with the assistance of Large Language Models (LLMs) for debugging and syntax correction. Additionally, the complete MATLAB script developed for the proposed B-GWO optimization framework and the CST co-simulation interface is provided as Supplementary Material.

2.3. Search Space Reduction and Symmetry Constraint

A massive combinatorial search space of size 2^N is formed using a pixel-based metasurface design (N is the overall number of pixels). In this paper, a Geometric Mirror Symmetry algorithm is applied to minimize the computational cost and maintain the physical symmetry of the MIMO system. The code architecture only defines 12 of the 24 pixels as active design variables. The pixel indexing map is shown in Figure 3. To reduce computational complexity, a Geometric Mirror Symmetry constraint is applied using a mapping relation:

$$P_i = P_{25-i}, \quad i \in \{13, \ldots, 24\} \tag{1}$$

where P_i represents the state (0 or 1) of the i-th pixel.

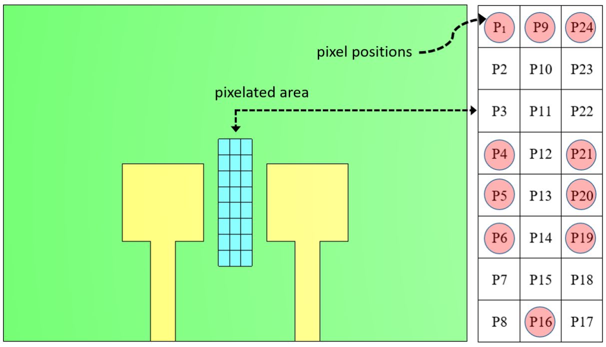

Figure 3. Proposed pixel indexing map and the implemented Geometric Mirror Symmetry principle.

This constraint ensures that the optimization algorithm only needs to solve for the first 12 pixels ($i = 1, \ldots, 12$), effectively halving the number of optimization variables. While eliminating asymmetric configurations restricts the mathematical diversity of the optimization solutions, enforcing mirror symmetry is a strict physical requirement in this design. An asymmetric decoupling structure would disrupt the port balance, leading to unequal reflection coefficients ($S_{11} \neq S_{22}$) and skewed radiation patterns, which severely degrades the MIMO system's diversity performance.

2.4. Binary GWO and Transfer Function

The traditional Grey Wolf Optimizer [37] operates in a continuous search space. However, the optimization of the pixelated metasurface is a discrete problem requiring binary values ("0" for air, "1" for copper). In this study, the continuous search space is bounded within the range $[0, 1]$. To map the continuous position vectors to binary space, an "S-shaped" Sigmoid transfer function is employed.

The continuous position value (x_i^d) of each search agent is converted into a probability value using the following equation:

$$T(x_i^d) = \frac{1}{1 + e^{-6(x_i^d - 0.5)}} \tag{2}$$

The final pixel state (X_i^d) is determined by comparing this generated probability value to a random number ($r \in [0, 1]$):

$$X_i^d = \begin{cases} 1, & \text{if } r < T(x_i^d) \\ 0, & \text{otherwise} \end{cases} \tag{3}$$

This method allows the algorithm to optimize a discrete topology without losing its ability to search in continuous space.

2.5. Cost Function and Penalty Mechanism

The primary goal of optimization involves two objectives: minimizing the mutual coupling (S_{21}) to improve isolation, and maintaining the reflection coefficients (S_{11}, S_{22}) below −10 dB. The cost function can be defined as a minimization problem. A dynamic

Penalty Mechanism is implemented in the MATLAB–CST interface in order to enforce the design constraints. The algorithm evaluates the maximum reflection coefficient (S_{11}, S_{22}) within the band. If this value exceeds the defined limit ($L_{\text{limit}} = -10$ dB), a heavy penalty is added to the cost function. The specific cost function used in this study, incorporating the dynamic penalty mechanism, is defined as follows:

$$Cost = \begin{cases} \max(S_{21}) + 10 \cdot (\max(S_{11}, S_{22}) - L_{limit}) + 100, & \text{if } \max(S_{11}, S_{22}) > L_{limit} \\ \max(S_{21}), & \text{otherwise} \end{cases} \quad (4)$$

where L_{limit} is the threshold for the reflection coefficient (set to -10 dB). This expanded form clearly shows how the penalty increases proportionally to the violation of the impedance matching constraint.

To maintain computational efficiency within the co-simulation loop, the cost function is formulated to minimize only the mutual coupling (S_{21}) with strict penalties applied to reflection coefficients (S_{11}, S_{22}). Explicitly optimizing the radiation gain or wideband behavior would require calculating 3D far-field monitors at every optimization iteration, which would significantly increase the simulation time to an impractical level. Instead, by strictly penalizing the reflection coefficients, the algorithm implicitly preserves the reference antenna's inherent broadband and gain characteristics without the need for multi-objective far-field optimization.

The configuration of the optimization process is summarized in detail in Table 2. A population of 12 search agents (wolves) was utilized to explore the binary search space over 20 iterations. To manage the computational cost, the search space was reduced from 24 bits to 12 bits by applying Geometric Mirror Symmetry. The optimization goal was defined by a cost function aimed at minimizing the mutual coupling (S_{21}) within the target band while maintaining the reflection coefficients (S_{11}, S_{22}) below -10 dB.

Table 2. Optimizationalgorithm settings and simulation parameters.

Parameter	Specification
Optimization Algorithm	Binary Grey Wolf Optimizer (B-GWO)
Simulation Environment	MATLAB–CST Co-Simulation
Number of Search Agents (Wolves)	12
Maximum Iterations	20
Control Parameter	Linearly decreases from 2 to 0
Total Number of Pixels	24 (Initial Design)
Optimization Dimension	12 Bits (Reduced via Mirror Symmetry)
Search Space Size	2^{12} (4096 combinations)
Frequency Range	26.5 GHz–29.5 GHz
Cost Function Goal	Minimize max (S_{21}) s.t. $S_{11}, S_{22} < -10$ dB

3. Results and Discussion

3.1. Optimization Process and Convergence

The systematic process of optimization is depicted in Figure 2. This is set up by a dynamic co-simulation connection between MATLAB and CST. In this loop, MATLAB plays the role of the optimization engine, creating the initial population of wolves (binary pixel configurations) and updating their current positions with the B-GWO algorithm. At each iteration, the resulting binary matrix is loaded into the CST solver through the ActiveX interface to restructure the pixelated metasurface into the physical structure. The electromagnetic solver then calculates the S-parameters (S_{11}, S_{21}, S_{22}), which are fed back to

MATLAB in order to evaluate the cost function. This process continues until the termination condition (maximum iterations) is attained.

The design of the decoupling surface was formulated as a binary optimization problem. The objective was to minimize mutual coupling by optimally determining the distribution of conductive pixels across the 3×8 grid. The proposed B-GWO algorithm was successfully deployed to navigate this discrete search space and resolve the optimization problem. The primary objective function of this optimization is defined as minimizing the maximum mutual coupling (S_{21}) across the operating frequency band (26.5 GHz to 29.5 GHz):

$$F(x) = \max(S_{21}(f)) \quad \text{for} \quad f \in [26.5, 29.5]\,\text{GHz} \tag{5}$$

However, to ensure impedance matching, this primary objective is expanded into a comprehensive cost function by incorporating penalty terms, as previously described in Equation (4). Figure 4 illustrates the convergence behavior of the B-GWO algorithm as it minimizes this penalized cost function during the optimization process.

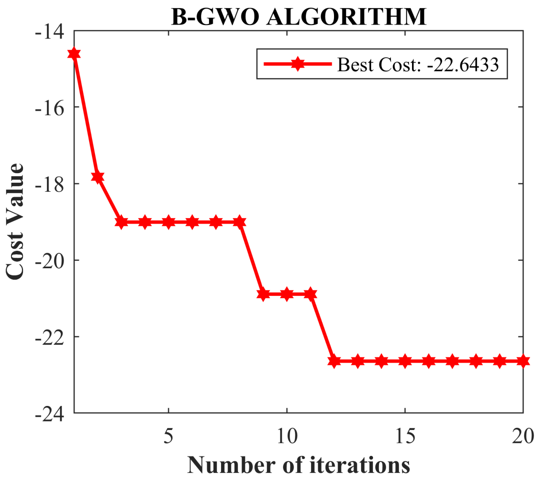

Figure 4. Convergence profile of the B-GWO algorithm throughout the optimization iterations.

As shown in Figure 4, the B-GWO algorithm exhibits an extremely rapid convergence rate. The initial random population has a cost value around −14.61 dB. The algorithm identifies the appropriate solution region for the first 12 iterations, depending on the search space reduction implemented by the Geometric Mirror Symmetry method. It stabilizes at a best cost of −22.64 dB and maintains this value throughout the remaining iterations. Locating an optimal solution region within such a short interval shows that the reduced search space helped the optimizer to converge quickly. This reduction also prevented the need for excessive computational time. The cost function represents the maximum mutual coupling over the entire band, whereas the specific resonance dip reaches −32.58 dB at 28.67 GHz. The computational efficiency is confirmed by this rapid stabilization, which provides high isolation performance without the need for excessive full-wave simulations.

Due to the heavy computational cost of the EM co-simulation, conducting a large number of independent runs is impractical. However, an additional independent validation run was performed to verify the repeatability of the B-GWO algorithm.

As shown in Table 3, while the validation run (Run 2) achieves slightly stronger in-band isolation (a peak S_{21} of −23.85 dB), it severely degrades the reflection profile, with the peak S_{11} reaching −12.33 dB. This value is dangerously close to the −10 dB operational threshold. In contrast, the proposed design (Run 1) provides a highly stable mutual coupling profile across the target band (peak S_{21} of −22.64 dB) while maintaining an excellent safety margin for reflection (peak S_{11} of −21.36 dB). Therefore, to ensure robust performance and resilience against manufacturing tolerances, the proposed design was deliberately selected as the optimal configuration for this study.

Table 3. Performance comparison of the optimization runs (26.5–29.5 GHz).

Optimization Run	Maximum Mutual Coupling (Peak S_{21})	Maximum Reflection (Peak S_{11} and S_{22})	In-Band Isolation Stability
Run 1 (Proposed Design)	−22.64 dB	−21.36 dB	Highly stable and flat
Run 2 (Validation)	−23.85 dB	−12.33 dB	Fluctuating profile

3.2. S-Parameter Analysis and Isolation

Before evaluating the proposed decoupling surface, it is necessary to establish the baseline performance of the reference UWB MIMO antenna (without any parasitic pixels). The simulated S-parameters for this reference case are presented in Figure 5a. Observing the reflection coefficients (S_{11}, S_{22}), it is evident that the design exhibits excellent impedance matching characteristics. As expected from the partial ground monopole topology, the antenna operates as a UWB radiator. The S_{11} and S_{22} values remain well below the −10 dB threshold across the entire simulated frequency range (22–34 GHz). Specifically, around the center frequency of the targeted 5G n257 band, the reflection coefficients (S_{11}, S_{22}) reach a minimum of −20.24 dB at 27.65 GHz, indicating highly efficient energy transfer from the feed line to the radiating element. This confirms that the standalone reference antenna is well-optimized.

The difficulty, however, is in the mutual coupling. The transmission coefficient plotted in Figure 5a indicates a major limitation within the target band of 26.5–29.5 GHz. As observed in the graph, the mutual coupling deteriorates toward the upper edge of the band, reaching a peak S_{21} of −14.67 dB at 29.5 GHz. This significant degree of coupling is mainly due to the close physical proximity of the elements and the high surface currents across the shared ground plane. Although the antenna has good efficiency, such crosstalk between ports would reduce the diversity gain and channel capacity of the MIMO system, which establishes the critical necessity for the proposed pixelated decoupling surface.

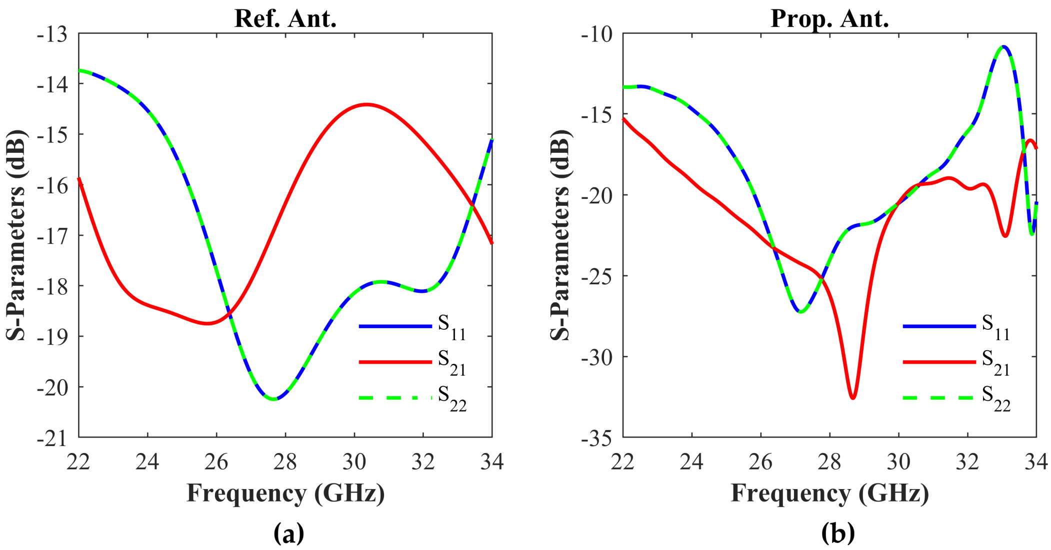

Figure 5. Simulated S-parameters of the (**a**) reference and (**b**) proposed MIMO antennas.

After the analysis of the baseline, the B-GWO-optimized pixelated surface was applied to the spacing between the elements. Figure 5b presents the S-parameter results of the proposed configuration. It is evident that the optimization has a significant impact on the transmission coefficient (S_{21}). The proposed design exhibits a sharp and deep isolation notch compared to the reference antenna, which, as previously established, suffered from high mutual coupling reaching a peak S_{21} of −14.67 dB at 29.5 GHz within the target band. The optimization targeted the entire 5G n257 band, successfully suppressing mutual coupling across this full range; 28.67 GHz is simply the point within this wide band where the maximum isolation (the deepest notch) of −32.58 dB is achieved. At this specific frequency, the reference antenna had a coupling level of −15.43 dB. When compared to the reference case, this represents a significant improvement of approximately 17.15 dB. Furthermore, the isolation is maintained above 20 dB across a wide frequency band (from 24.5 GHz to 30.2 GHz), completely covering the intended 5G n257 band. This wideband suppression demonstrates that the pixelated surface works effectively as a robust band-stop filter.

A common drawback of integrating parasitic elements is the potential degradation of impedance matching. However, the proposed design mitigates this issue by preserving the UWB characteristics, as illustrated by the reflection coefficient curves (S_{11} and S_{22}). It is evident that the reflection coefficients remain below −10 dB across the entire 22–34 GHz band. In particular, the addition of the pixelated structure shifts the resonance dip from 27.65 GHz to 27.16 GHz and deepens it, reaching −27.24 dB. This demonstrates that the B-GWO algorithm optimized the parasitic structure for high isolation while adaptively adjusting it to secure and enhance the energy transfer efficiency of the monopole elements. Hence, decoupling of the MIMO ports is successfully achieved by converting the reference design into the proposed architecture.

3.3. Surface Current Distribution Analysis

To explain the physical mechanism behind the isolation concept, the surface current distributions at the resonance frequency of 28 GHz are analyzed. Figure 6a and Figure 6b present the simulated results for the reference and proposed antennas, respectively. Port 1 is excited while Port 2 is terminated with a 50 Ω matched load.

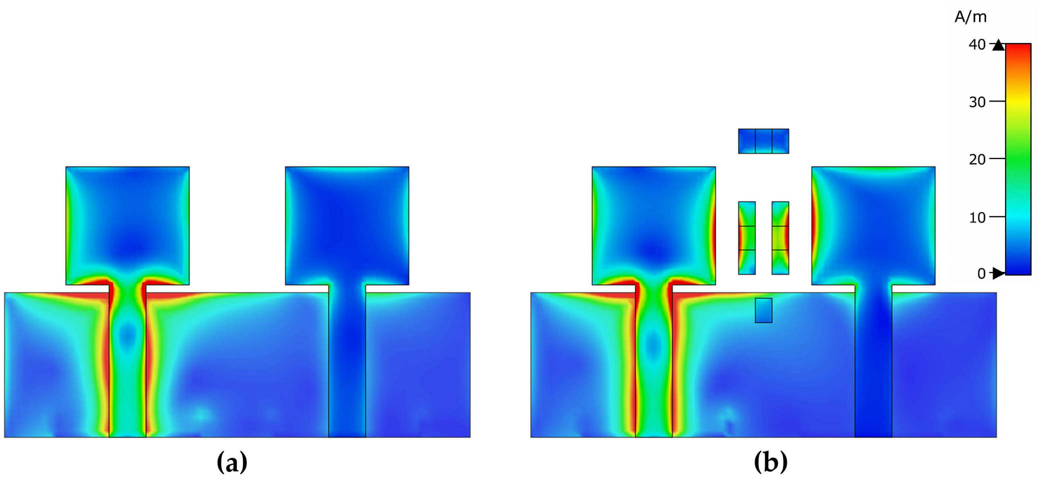

Figure 6. Surface current distributions at 28 GHz: (**a**) reference antenna; (**b**) proposed antenna.

In the reference antenna shown in Figure 6a, it is clearly observed that surface currents strongly propagate across the common ground plane. As observed in the reference design, these currents migrate across the separation gap and excite substantial energy levels on the passive port's feed line, thereby validating the presence of a direct electromagnetic coupling route. Conversely, the configuration depicted in Figure 6b highlights the operational success of the integrated decoupling architecture. The pixelated surface, specifically refined through the B-GWO routine, functions as a physical and electromagnetic shield. By behaving as a localized band-stop resonator, the conductive pixel grid captures the surface waves navigating the minimal distance between ports and effectively traps this energy within the pixelated domain. This confinement prevents the unwanted transfer of power, ensuring that the radiated fields remain isolated. As a result, the surface current density on the passive element (Port 2) is minimized. Moreover, the central pixels contain the most significant current loops as they are close to the coupling path, whereas the periphery pixels assist in maintaining the resonance stability. Crucially, although a high current density is observed on the edges of the passive patch in Figure 6b, this represents reactive stored energy (standing waves) rather than transmission. The definitive proof of isolation is observed in the feed line of the second port, which remains dark blue (low current density). This confirms that the trapped energy does not couple to the fundamental mode of the feed line, effectively blocking the signal transmission to the output port.

3.4. Radiation Performance Analysis

The main issue of concern in the decoupling surface design is the fact that adding parasitic elements may reduce the far-field radiation performance of the antenna. To ensure that the proposed design is efficient in radiation, we compared the radiation patterns and the realized gain of the reference and proposed antennas. Figure 7 illustrates the simulated 2-D polar radiation patterns in the E-plane ($\phi = 0°$) and H-plane ($\theta = 90°$) at the center frequency of 28 GHz. Since the MIMO antenna system is geometrically symmetric, the radiation patterns for Port 2 are mirror images of Port 1. Therefore, only the results for Port 1 are presented.

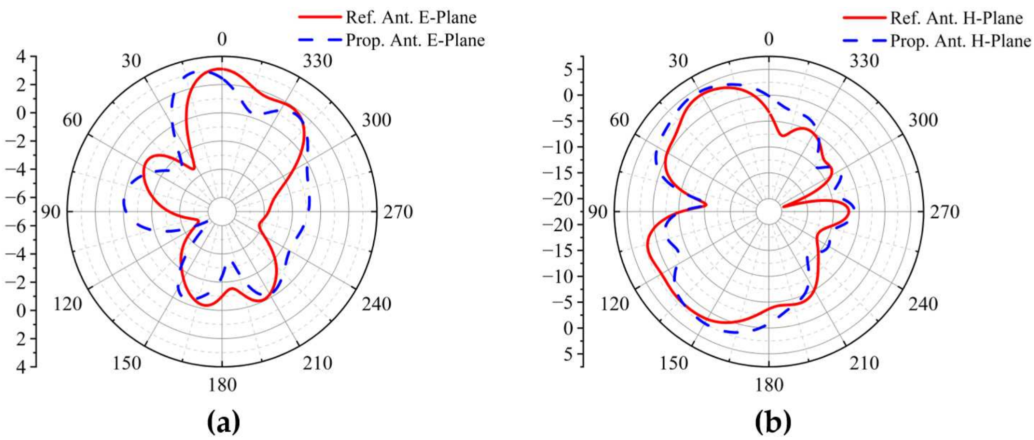

Figure 7. Comparison of the radiation patterns at 28 GHz: (**a**) E-Plane ($\phi = 0°$); (**b**) H-Plane ($\theta = 90°$).

In the case of Figure 7a, it is observed that the reference antenna (red curve) has a bidirectional radiation pattern typical of planar monopoles. Notably, in the proposed antenna (blue dashed curve), this radiation profile is well-preserved. It is observed that when the pixelated surface is included in the near-field region, it does not deteriorate the main radiation beam. The antenna retains its effective radiation properties, although minor distortions and a slight inclination in the main lobe are observed due to the asymmetric loading of the parasitic pixels. More importantly, the primary beamwidth is not compromised, but rather, is somewhat improved. This reaffirms that the enhancement in isolation is achieved by the suppression of surface waves, which in turn aids in directing more energy into free space.

The radiation pattern in the H-plane (Figure 7b) is not perfectly omnidirectional; instead, it exhibits a distorted shape with observable nulls at 90° and 270°. This is the expected physical behavior in a MIMO configuration due to the shadowing effect of the adjacent passive element (Port 2), which acts as a reflector or blocker in the horizontal plane. In comparison to the reference antenna (red curve), the proposed design (blue dashed curve) closely follows the original profile without any gain reduction. In fact, the proposed antenna exhibits slightly higher gain in certain angular directions (e.g., 30°–60°) as a result of the constructive interference of the scattered fields from the pixels.

The agreement between the reference and proposed patterns proves that the B-GWO-optimized surface functions effectively as a surface wave suppressor. It eliminates leakage current between the ports without hampering the electromagnetic fields radiating from the antenna. Consequently, high isolation is obtained without compromising the far-field coverage of the MIMO system.

3.5. Realized Gain

Figure 8 illustrates the 3D realized gain radiation patterns of the reference antenna (a) and the proposed antenna (b). A common challenge with decoupling designs is the degradation of radiation efficiency due to the additional loading on the metasurface. However, the proposed design demonstrates a significant improvement in radiation performance.

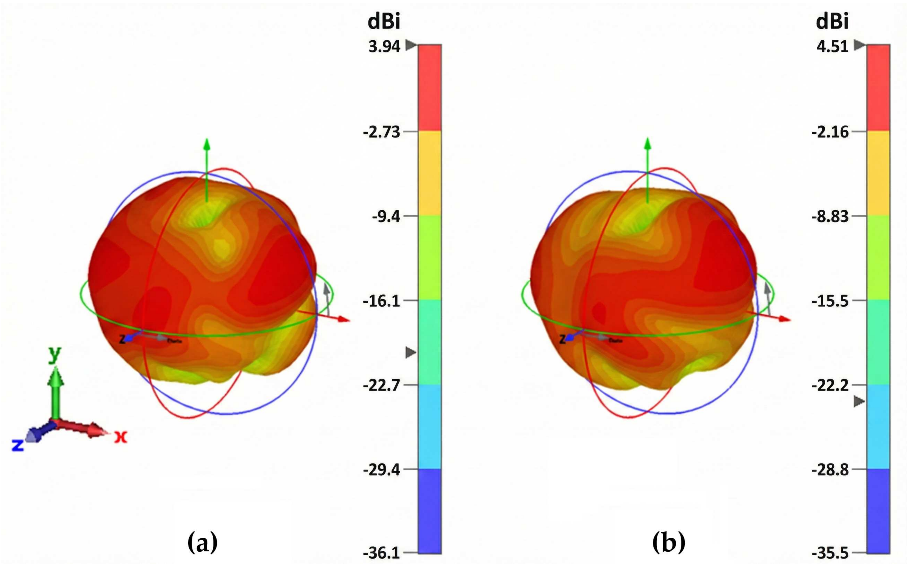

Figure 8. Realized gain radiation patterns at 28 GHz: (**a**) reference antenna without decoupling structure; (**b**) proposed antenna with decoupling structure.

A detailed examination of the 3D radiation results in Figure 8 reveals that the reference monopole configuration provides a maximum realized gain of 3.94 dBi. Upon integrating the GWO-optimized pixelated metasurface, this value rises to 4.51 dBi at the 28 GHz resonance frequency. This 0.57 dB gain increment stems directly from the successful containment of surface waves within the decoupling layer. By effectively obstructing the leakage currents that would otherwise migrate to the neighboring port, the proposed structure minimizes both substrate-level and coupling-related losses. This mechanism forces a more efficient redirection of electromagnetic energy toward the primary radiation lobe. Consequently, the pixelated design serves a dual purpose: achieving superior port isolation while simultaneously enhancing the realized gain of the MIMO antenna system. To further validate the preservation of radiation performance, the radiation efficiency was evaluated at 28 GHz. The reference antenna achieves a radiation efficiency of 95.8%, while the proposed MIMO antenna maintains a highly robust efficiency of 95.6%. This confirms that the introduced metasurface does not act as a lossy resistive load, ensuring no significant efficiency degradation in the overall system.

3.6. Equivalent Circuit Model (ECM) Validation

To rigorously validate the proposed decoupling mechanism, the scattering parameters obtained from CST were compared with the theoretical results derived from the Equivalent Circuit Model (ECM). The observed agreement demonstrates that the behavior of the pixelated metasurface is accurately characterized by the proposed equivalent circuit network.

The topology of the developed ECM is depicted in Figure 9, and the extracted lumped element parameters are listed in Table 4.

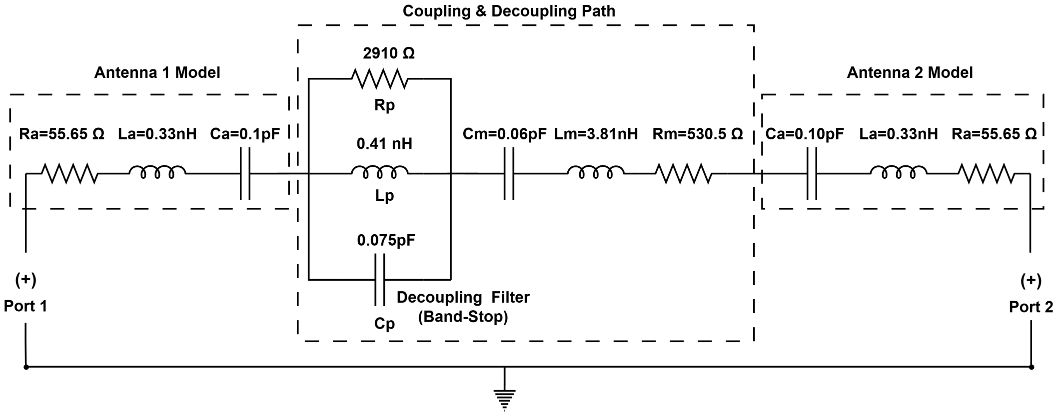

Figure 9. Equivalent Circuit Model (ECM) of the proposed MIMO antenna.

Table 4. Extracted equivalent circuit parameters.

Parameter	Description	Value (Proposed)
R_a (Ω)	Antenna Resistance	55.65
L_a (nH)	Antenna Inductance	0.33
C_a (pF)	Antenna Capacitance	0.10
R_m (Ω)	Mutual Resistance	530.5
L_m (nH)	Mutual Inductance	3.81
C_m (pF)	Mutual Capacitance	0.06
L_p (nH)	Pixel Inductance	0.41
C_p (pF)	Pixel Capacitance	0.075
R_p (Ω)	Pixel Resistance	2910

The full-wave simulation results demonstrate a strong correlation with the extracted circuit model, as presented in Figure 10. While a simplified RLC network is employed to estimate the average coupling level of the reference antenna (ignoring minor fluctuations), the sharp resonance characteristics of the proposed decoupling structure are accurately captured. Notably, a frequency shift is observed; the introduction of the pixelated surface induces a capacitive loading effect, shifting the resonance frequency (S_{11}) from 27.65 GHz (reference) to 27.16 GHz (proposed). This shift is accurately tracked by the circuit model (dashed blue line), confirming that the extracted inductance (L) and capacitance (C) values validly represent the physical impedance of the antenna structure.

The most critical validation is observed in the isolation characteristics (S_{21}) depicted in Figure 10b. The sharp transmission zero of the proposed design demonstrates a distinct notch characteristic at the target frequency of 28.67 GHz. Both the Equivalent Circuit Model and full-wave simulation results exhibit excellent agreement regarding the resonance frequency and the level of isolation enhancement. This close correspondence between the field-based (CST) and circuit-based (ECM) results confirms that the pixelated metasurface functions effectively as a band-stop LC filter. By suppressing surface wave propagation at the resonance frequency, it prevents coupling to the adjacent port.

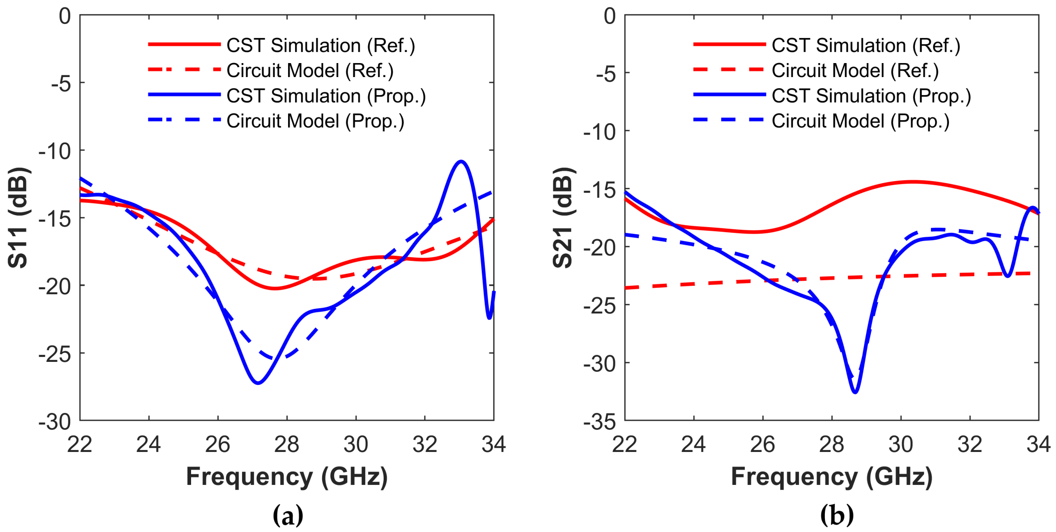

Figure 10. Comparison of S-parameters between full-wave simulation (solid lines) and Equivalent Circuit Model (dashed lines): (**a**) reflection coefficient (S_{11}); (**b**) isolation (S_{21}).

4. MIMO Diversity Performance Analysis

4.1. Envelope Correlation Coefficient

The Envelope Correlation Coefficient (ECC) illustrated in Figure 11 is employed to evaluate the independence of the antenna elements within the MIMO system. It is calculated using the scattering parameters (S-parameters), as expressed in the following equation:

$$\mathrm{ECC} = \rho_e = \frac{|S_{11}^* S_{12} + S_{21}^* S_{22}|^2}{(1 - (|S_{11}|^2 + |S_{21}|^2))(1 - (|S_{22}|^2 + |S_{12}|^2))} \tag{6}$$

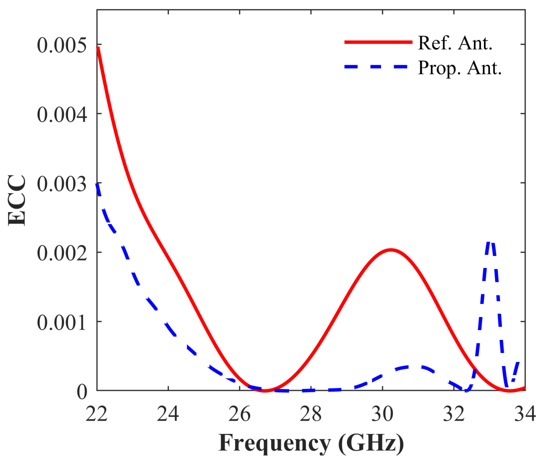

Figure 11. Calculated Envelope Correlation Coefficient (ECC).

As shown in Figure 11, the ECC values are extremely low through the entire ultra-wideband range. In particular, in the 5G n257 band, the ECC is less than 0.002, which is significantly lower than the operational target of 0.5. This demonstrates that there is high pattern diversity in the two ports and the signals are not correlated.

4.2. Diversity Gain (DG)

Based on the calculated values of ECC, the diversity gain (DG) was calculated based on the relation $DG = 10\sqrt{1 - |\rho_e|^2}$. The DG is determined to be 9.99 dB across the operating band, and this is close to the theoretical maximum of 10 dB since the correlation is found to be almost zero. This will make the proposed MIMO system capable of reducing the multipath fading effects.

4.3. Total Active Reflection Coefficient (TARC)

In order to determine the stability of the MIMO system when it is simultaneously excited, the Total Active Reflection Coefficient (TARC) was determined. TARC compares the total reflected power with the total incident power and is important in the verification of impedance matching in a multi-port environment. The TARC is calculated using the standard relation for a two-port MIMO system:

$$\text{TARC} = \Gamma_a^t = \sqrt{\frac{\left|S_{11} + S_{12}e^{j\theta}\right|^2 + \left|S_{21} + S_{22}e^{j\theta}\right|^2}{2}} \tag{7}$$

As can be seen in Figure 12, the TARC value does not exceed the -10 dB threshold at any point in the whole frequency spectrum of 22–34 GHz. This confirms that the proposed MIMO antenna maintains excellent impedance matching and stable performance even when both ports are simultaneously excited with random phase differences.

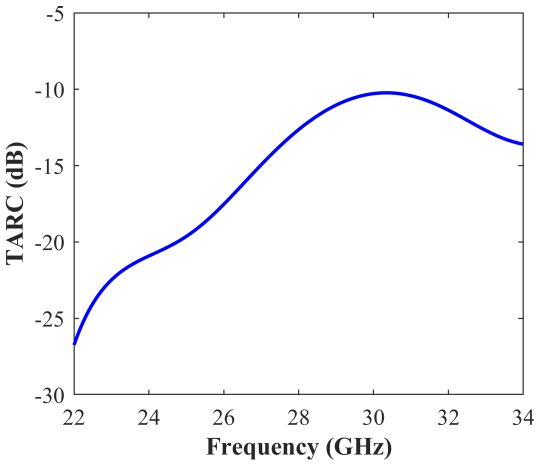

Figure 12. Calculated Total Active Reflection Coefficient (TARC).

5. Conclusions

This paper proposes a computational design strategy based on the Binary Grey Wolf Optimizer (B-GWO) to develop a high-isolation MIMO antenna system suitable for 5G mm-Wave applications. To mitigate mutual coupling, a pixelated metasurface functioning as a band-stop resonator was optimized and integrated between the antenna elements. The full-wave simulation results demonstrate that the proposed decoupling structure effectively suppresses surface wave propagation, thereby reducing the mutual coupling level from -15.43 dB to -32.58 dB at 28.67 GHz. This improvement was validated using both surface current analysis and an Equivalent Circuit Model (ECM). The close agreement between circuit theory and electromagnetic simulations confirms that the pixelated structure acts as a high-impedance blocking filter across the operational band. Moreover, one of the most important contributions of this work is the improvement in radiation performance. The proposed design maximizes the peak realized gain to 4.51 dBi, which is 0.57 dB higher than that of the reference antenna, avoiding the insertion losses often observed in conventional decoupling methods. Consequently, the proposed antenna system offers a compact, validated, and energy-efficient design with excellent diversity performance (ECC < 0.005 and TARC < -10 dB), making it highly suitable for dense 5G arrays.

It should be noted that the findings presented in this study are fundamentally computational and theoretical, validated through full-wave electromagnetic simulations and rigorous ECM analysis. While the proposed B-GWO-optimized pixelated metasurface demonstrates excellent and stable theoretical isolation across the target n257 band (26.5–29.5 GHz), this research currently serves as a methodological computational design framework. Future work will focus on the physical fabrication and experimental measurement of the optimized MIMO prototype to investigate the effects of manufacturing tolerances, substrate losses, and real-world deployment challenges at mm-Wave frequencies.

Supplementary Materials: The following supporting information can be downloaded at: https://www.mdpi.com/article/10.3390/electronics15081625/s1, Algorithm S1: The MATLAB source code for the Binary Grey Wolf Optimizer (B-GWO) algorithm interfacing with CST Studio Suite.

Author Contributions: Conceptualization, M.Ü., M.K., L.W. and O.A.; methodology, M.Ü., M.K., L.W., A.A. and O.A.; validation, M.Ü. and M.K.; writing—original draft preparation, M.Ü., M.K., L.W., A.A. and O.A.; data curation, M.Ü.; software, M.Ü.; supervision, M.K.; investigation, M.Ü., M.K., L.W., A.A. and O.A.; visualization, M.Ü., A.A. and O.A. All authors have read and agreed to the published version of the manuscript.

Funding: This research received no external funding.

Data Availability Statement: The data presented in this study are available within the article. The MATLAB scripts used for the optimization and simulation processes are available in the Supplementary Materials.

Acknowledgments: The core logical design and optimization routine were developed independently by the authors to ensure the study's originality. Subsequently, Large Language Models (Gemini PRO and ChatGPT-5) were utilized solely to assist in debugging, refining the syntax of the MATLAB scripts, and improving the grammatical structure and readability of the manuscript. The authors have meticulously reviewed and edited all AI-assisted refinements and take full responsibility for the final code and the integrity of this publication.

Conflicts of Interest: The authors declare no conflicts of interest.

Abbreviations

The following abbreviations are used in this manuscript:

B-GWO	Binary Grey Wolf Optimizer
CST	Computer Simulation Technology
DG	Diversity Gain
ECC	Envelope Correlation Coefficient
ECM	Equivalent Circuit Model
LLM	Large Language Model
MIMO	Multiple-Input Multiple-Output
mm-Wave	Millimeter Wave
RLC	Resistor–Inductor–Capacitor
TARC	Total Active Reflection Coefficient
UWB	Ultra-Wideband

References

1. Chowdhury, M.Z.B.; Islam, M.T.; Hossain, I.; Samsuzzaman, M. A compact 6-shaped high isolation MIMO antenna for 28 GHz 5G applications. *Int. J. Commun. Syst.* **2025**, *38*, e5991. [CrossRef]
2. Przesmycki, R.; Bugaj, M.; Nowosielski, L. Broadband Microstrip Antenna for 5G Wireless Systems Operating at 28 GHz. *Electronics* **2020**, *10*, 1. [CrossRef]
3. Iqbal, A.; Basir, A.; Smida, A.; Mallat, N.K.; Elfergani, I.; Rodriguez, J.; Kim, S. Electromagnetic Bandgap Backed Millimeter-Wave MIMO Antenna for Wearable Applications. *IEEE Access* **2019**, *7*, 111135–111144. [CrossRef]
4. Manage, P.S.; Naik, U.; Rayar, V. Optimization Algorithms for MIMO Antennas: A Systematic Review. *Wirel. Pers. Commun.* **2023**, *131*, 105–139. [CrossRef]

5. Elalaouy, O.; El Ghzaoui, M.; Foshi, J. Mutual coupling reduction of a two-port MIMO antenna using defected ground structure. *e-Prime-Adv. Electr. Eng. Electron. Energy* **2024**, *8*, 100557. [CrossRef]
6. Khalid, M.; Naqvi, S.I.; Hussain, N.; Rahman, M.; Fawad; Mirjavadi, S.S.; Khan, M.J.; Amin, Y. 4-Port MIMO Antenna with Defected Ground Structure for 5G Millimeter Wave Applications. *Electronics* **2020**, *9*, 71. [CrossRef]
7. Bhattacharya, A.; Roy, B.; Chowdhury, S.K.; Bhattacharjee, A.K. Computational and experimental analysis of a low-profile, isolation-enhanced, band-notch UWB-MIMO antenna. *J. Comput. Electron.* **2019**, *18*, 680–688. [CrossRef]
8. Rao, J.; Ming, Z.; Zhang, J.; Li, Z.; Chiu, C.Y.; Murch, R. A Compact Shared-Aperture Antenna with 2-Transmit and 2-Receive Highly-Isolated Ports for Full-Duplex MIMO Systems. *IEEE Open J. Antennas Propag.* **2025**, *6*, 422–432. [CrossRef]
9. Wu, K.L.; Wei, C.; Mei, X.; Zhang, Z.Y. Array-Antenna Decoupling Surface. *IEEE Trans. Antennas Propag.* **2017**, *65*, 6728–6738. [CrossRef]
10. Ahmed, A.; Kumari, V.; Sheoran, G. Reduction of mutual coupling in antenna array using metamaterial surface absorber. *AEU-Int. J. Electron. Commun.* **2023**, *160*, 154519. [CrossRef]
11. Li, M.; He, Y.; Zhou, C.; Zhang, Y.; Wu, D. Design of Decoupling and Pattern Shaping Surface for MIMO Antennas Using the Multiport Optimization Method. *IEEE Trans. Antennas Propag.* **2025**, *73*, 2927–2939. [CrossRef]
12. Zhang, Y.; Tang, S.; Yang, P.; Yin, T.; Chen, X. An Integrated Radiating and Decoupling Surface for MIMO Antenna Array. *IEEE Antennas Wirel. Propag. Lett.* **2025**, *24*, 4222–4226. [CrossRef]
13. Rao, J.; Zhang, Y.; Tang, S.; Li, Z.; Shen, S.; Chiu, C.Y.; Murch, R. A Novel Reconfigurable Intelligent Surface for Wide-Angle Passive Beamforming. *IEEE Trans. Microw. Theory Tech.* **2022**, *70*, 5427–5439. [CrossRef]
14. Ghewari, P.; Patil, V. Advancements in Microstrip Patch Antenna Design Using Nature-Inspired Metaheuristic Optimization Algorithms: A Systematic Review. *Arch. Comput. Methods Eng.* **2025**, *32*, 3687–3732. [CrossRef]
15. Wu, Q.; Chen, W.; Yu, C.; Wang, H.; Hong, W. Machine-Learning-Assisted Optimization for Antenna Geometry Design. *IEEE Trans. Antennas Propag.* **2024**, *72*, 2083–2095. [CrossRef]
16. Liu, B.; Aliakbarian, H.; Ma, Z.; Vandenbosch, G.A.E.; Gielen, G.; Excell, P. An Efficient Method for Antenna Design Optimization Based on Evolutionary Computation and Machine Learning Techniques. *IEEE Trans. Antennas Propag.* **2014**, *62*, 7–18. [CrossRef]
17. Melo, M.C.D.; Santos, P.B.; Faustino, E.; Bastos-Filho, C.J.A.; Cerqueira Sodré, A. Computational Intelligence-Based Methodology for Antenna Development. *IEEE Access* **2022**, *10*, 1860–1870. [CrossRef]
18. Li, X.; Luk, K.M. The Grey Wolf Optimizer and Its Applications in Electromagnetics. *IEEE Trans. Antennas Propag.* **2020**, *68*, 2186–2197. [CrossRef]
19. Song, C.; Pan, L.; Jiao, Y.; Jia, J. A High-Performance Transmitarray Antenna with Thin Metasurface for 5G Communication Based on PSO (Particle Swarm Optimization). *Sensors* **2020**, *20*, 4460. [CrossRef]
20. Nath, G.V.; Ram, G.; Subhashini, K.R. Thinned planar antenna array synthesis using a hybrid approach combining almost difference sets and weighted total least squares method. *AEU-Int. J. Electron. Commun.* **2023**, *172*, 154943. [CrossRef]
21. Kovaleva, M.; Bulger, D.; Esselle, K.P. Cross-Entropy Method for Design and Optimization of Pixelated Metasurfaces. *IEEE Access* **2020**, *8*, 224922–224931. [CrossRef]
22. Kiziltas, G.; Psychoudakis, D.; Volakis, J.L.; Kikuchi, N. Topology design optimization of dielectric substrates for bandwidth improvement of a patch antenna. *IEEE Trans. Antennas Propag.* **2003**, *51*, 2732–2743. [CrossRef]
23. Ullah, M.A.; Keshavarz, R.; Abolhasan, M.; Lipman, J.; Shariati, N. Multiservice Compact Pixelated Stacked Antenna with Different Pixel Shapes for IoT Applications. *IEEE Internet Things J.* **2023**, *10*, 19883–19897. [CrossRef]
24. Ullah, M.A.; Keshavarz, R.; Abolhasan, M.; Lipman, J.; Shariati, N. Low-profile dual-band pixelated defected ground antenna for multistandard IoT devices. *Sci. Rep.* **2022**, *12*, 11479. [CrossRef]
25. Ghadimi, A.; Nayyeri, V.; Khanjarian, M.; Soleimani, M.; Ramahi, O.M. A Systematic Approach for Mutual Coupling Reduction Between Microstrip Antennas Using Pixelization and Binary Optimization. *IEEE Antennas Wirel. Propag. Lett.* **2020**, *19*, 2048–2052. [CrossRef]
26. Zhou, Z.; Cheng, Z.; Su, Z.; Li, M.; Zhang, Z.; Ge, Y.; Gao, Y.; Xie, W.; David Chen, Z. Pixel-Metastructure-Assisted Subarray Decoupling for Compact MIMO Antenna Designs. *IEEE Trans. Antennas Propag.* **2025**, *73*, 10161–10171. [CrossRef]
27. Rodrigo, D.; Cetiner, B.A.; Jofre, L. Frequency, Radiation Pattern and Polarization Reconfigurable Antenna Using a Parasitic Pixel Layer. *IEEE Trans. Antennas Propag.* **2014**, *62*, 3422–3427. [CrossRef]
28. Zheng, W.; Li, H. Designing Antennas with Quasi-Isotropic Radiation Patterns Using Pixel Structures. *IEEE Trans. Antennas Propag.* **2023**, *71*, 7813–7823. [CrossRef]
29. Jiang, F.; Shen, S.; Chiu, C.Y.; Zhang, Z.; Zhang, Y.; Cheng, Q.S.; Murch, R. Pixel Antenna Optimization Based on Perturbation Sensitivity Analysis. *IEEE Trans. Antennas Propag.* **2022**, *70*, 472–486. [CrossRef]
30. Song, S.; Murch, R.D. An Efficient Approach for Optimizing Frequency Reconfigurable Pixel Antennas Using Genetic Algorithms. *IEEE Trans. Antennas Propag.* **2014**, *62*, 609–620. [CrossRef]
31. Qiao, T.; Jiang, F.; Shen, S.; Zhang, Z.; Li, M.; Chiu, C.Y.; Cheng, Q.S.; Murch, R. Pixel Antenna Optimization Using the Adjoint Method and the Method of Moving Asymptote. *IEEE Trans. Antennas Propag.* **2023**, *71*, 2873–2878. [CrossRef]

32. Soltani, S.; Lotfi, P.; Murch, R.D. Design and Optimization of Multiport Pixel Antennas. *IEEE Trans. Antennas Propag.* **2018**, *66*, 2049–2054. [CrossRef]
33. Jiang, F.; Zhang, Z.; Li, M.; Shen, S.; Chiu, C.Y.; Zhang, Y.; Cheng, Q.S.; Murch, R. Multiport Pixel Antenna Optimization Using Characteristic Mode Analysis and Sequential Feeding Port Search. *IEEE Trans. Antennas Propag.* **2022**, *70*, 9160–9174. [CrossRef]
34. Liu, B.; Wu, T.; Wong, K.K.; Wong, H.; Tong, K.F. Wideband Pixel-Based Fluid Antenna System: An Antenna Design for Smart City. *IEEE Internet Things J.* 2025, *early access*. [CrossRef]
35. Zhang, J.; Rao, J.; Li, Z.; Ming, Z.; Chiu, C.Y.; Wong, K.K.; Tong, K.F.; Murch, R. A Novel Pixel-Based Reconfigurable Antenna Applied in Fluid Antenna Systems with High Switching Speed. *IEEE Open J. Antennas Propag.* **2025**, *6*, 212–228. [CrossRef]
36. Pan, Y.; Dong, J.; Luo, H.; Wang, M.; Xiao, C. Phase Cancellation-Assisted BGWO Method for Advanced Design of Ultrawideband RCS Reduction Metasurface. *IEEE Trans. Microw. Theory Tech.* **2025**, *73*, 7351–7362. [CrossRef]
37. Mirjalili, S.; Mirjalili, S.M.; Lewis, A. Grey Wolf Optimizer. *Adv. Eng. Softw.* **2014**, *69*, 46–61. [CrossRef]